Forward Modeling Chromatic Aberration and Depth of Field in Transmission X-ray Microscopy

Zane Taylor

Abstract—In this work, a computationally cheap algorithm is proposed for forward modeling defocusing blur and chromatic aberration for arbitrary illumination spectra in transmission x-ray microscopes. This method assumes the microscope is not diffraction limited, such that the depth-dependent blur kernel is Gaussian. This construction is based on ray optics and neglects the influence of interference and refraction in the sample. The result is intuitive, gives information about a focal stack of monochromatic images, and captures the chromaticity of compound refractive lenses in the x-ray regime. Work remains to compare these findings to more computationally intensive wave-optics simulations and experimental results.

Index Terms—Transmission X-ray Microscopy, Depth of Field, Chromatic Aberration

1 Introduction

LASER powder bed fusion (LPBF) is a metal additive manufacturing technique which uses high power lasers to selectively melt and fuse metal powders together into parts of near arbitrary geometry. This geometric freedom has made LPBF and related technologies pivotal to improving part performance and efficiency in fields such as aerospace, biomedicine, energy, and defense. Due to the highly dynamic nature of LPBF physics and the life-threatening consequences of part failure, an understanding of these chaotic physics and underlying defect mechanisms is critical. Synchrotron-based operando x-ray imaging in the form of high-speed radiography (lensless imaging) is the established workhorse technique in studying these physical processes, but is limited in resolution [1], [2], [3], [4], [5], [6].

We recently demonstrated operando transmission x-ray microscopy (TXM) at x-ray free electron lasers (XFELs) as a powerful new technique to study LPBF with temporal and spatial resolution improved by orders of magnitude.

Two important questions arise in the consideration of TXM and the development of more advanced microscopes:

- How large is the depth of field and how is resolution impacted by defocusing?
- How significant are chromatic aberrations?

TXM can be built upon a wide variety of x-ray lenses, but the simplest are compound refractive lenses (CRLs), which are notable for being highly chromatic. This chromaticity is the critical reason why high-speed TXM cannot be implemented at a synchrotron. Synchrotrons provide high fluence, but their bandwidth is too large, so the beam needs to be monochromated prior to imaging, which results in an effective fluence that is too low for operando imaging. XFELs, in contrast, offer much greater peak brilliance and lower native bandwidths that avoid this monochromation issue [7]. For this reason, our experiment was able to implement TXM without any beam monochromation and obtained unparalleled resolution in the field of operando LPBF studies.

- *Z. Taylor is with the Department of Materials Science and Engineering, Stanford University, Pasadena, CA, 94305.*
E-mail: zwtaylor@stanford.edu

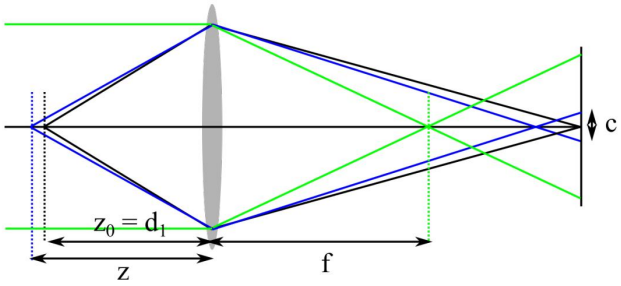

Fig. 1. Ray optics argument for the circle of confusion.

However, XFELs are not perfectly monochromatic and their finite bandwidth can still contribute to chromatic aberration and blurring, as well as shifts in the focal position that result in varying defocus through the sample as a function of photon energy.

This work will construct a simple formalism to calculate an anticipated image as a result of chromatic aberrations and defocusing. These calculations will be tied to the known physics of CRL-based microscopes and will consider chromatic aberration in such a way that the contribution of arbitrary source spectra can be accounted.

2 Related Work

2.1 Optical Models of Defocusing Blur

Blurring is typically described in terms of the point spread function or PSF. In the context of defocusing or depth of field, blurring has been described in many ways. In the diffraction limit, the PSF is decribed by a $circ$ function, creating the Airy disk in Fourier space, but far from the diffraction limit, the PSF is usually modeled as a z-dependent Gaussian kernel [9], [10].

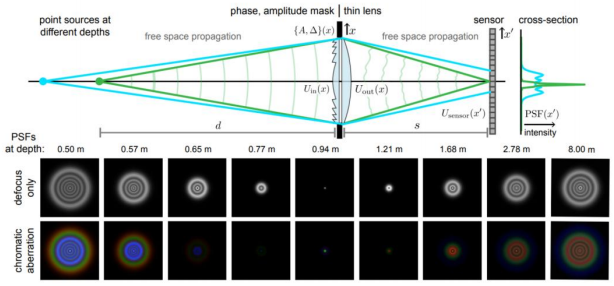

Fig. 2. Diffraction limited PSF due to defocusing. Figure taken without permission from [8]

Using conventional ray optics, the circle of confusion introduced by defocusing is given by

$$c = \frac{Af}{z_0 - f} \cdot \frac{z - z_0}{z} \tag{1}$$

where A is the aperture diameter of the lens, f is the focal length, z_0 is the focal plane (sample to lens distance), and z is the actual feature position.

Similarly, if a minimum acceptable circle of confusion, c_{thresh}, is defined, then the depth of field is defined by

$$DoF = 2\frac{fc_{thresh}}{A} \cdot \frac{M+1}{M^2 - \left(\frac{c_{thresh}}{A}\right)^2} \tag{2}$$

where M is the magnification of the imaging system [11]. The geometric arguments for this are shown in Figure 1, where an experimentally measured PSF is shown with defocusing is shown in Figure 2.

2.2 Optical Models of Chromaticity

In the optical regime, chromaticity can be modelled by color-channel based image warping or integration over wavelengths using a forward model of the imaging system [12], [13], [14].

2.3 CRL Behavior

Simons et al. [15] derived the behavior of CRLs using ray optics under the paraxial approximation. This formalism recovers a thick lens equation

$$\frac{1}{d_1} + \frac{1}{d_2} - \frac{1}{f_N} + \frac{f\phi\tan(N\phi)}{d_1 d_2} = 0 \tag{3}$$

where d_1, d_2, and $f_N = f\phi\cot(N\phi)$ respectively define the distance between the sample and the front of the CRL, the distance between the back of the CRL and the detector, and the CRL's effective focal length. These are in turn defined by lens properties including the focal length of each individual lenslet, $f = R/2\delta$, a geometric term $\phi = (T/f)^{1/2}$, and the number of lenslets, N. Here, δ is the refractive decriment ($n = 1 - \delta + i\beta$), R is the radius of curvature of a lenslet, and T is the distance between lenslets.

Given some sample to detector distance $L = d_1 + d_2 + NT$, and these defining properties, the magnification of the microscope is obtained by solving the following equation for M

$$N = \frac{1}{\phi}\left[\sin^{-1}\left(\frac{M + 1/M}{\{(L - NT)/f\phi\} + 4^{1/2}}\right) + \tan^{-1}\left(\frac{2f\phi}{L - NT}\right)\right] \tag{4}$$

With this magnification defined in a general case, the microscope positions can be obtained by evaluating,

$$d_1 = f_N\left[1 + \frac{1}{M\cos(N\phi)}\right] \tag{5}$$

$$d_2 = f_N\left[1 + \frac{M}{cos(N\phi)}\right] \tag{6}$$

As has been mentioned, CRLs are highly chromatic because of their sensitive energy dependence to δ in the x-ray regime.

Simons et al. [15] went on to derive the chromatic PSF by integrating an energy-depended PSF over a Gaussian distributed spectrum to obtain

$$PSF_{ch} = I_0 \exp\left(\frac{-|y_s|}{\sigma_e \sigma_a M d_{ch}}\right) \tag{7}$$

with y_s being the radial position of the ray from the center of the CRL, σ_e being the standard deviation of the Gaussian distributed spectrum of the imaging beam, σ_a being the angular acceptance of the imaging system, and d_{ch} is the effective (energy dependent) shift in the imaging system length.

The primary limitation with this formalism is that energy-dependent changes in the image are integrated out and the spectrum is assumed. This prevents their model from accounting for the effects of things like prisms and filters which change the imaging spectrum or further modify the image in a chromatic fashion. This approach also neglects considerations of defocusing blur if considered alone.

3 Proposed Method

In the proposed method outlined in Figure 3, a sample will be defined by $\Gamma \in \mathbb{R}^{(H,W,S)}$ where the entries $\Gamma(x, y, z) \in [0, 1]$ define the transmission through any given voxel. A perfectly in-focus imaging system would give a result which simply integrates along the z-dimension:

$$I_{perfect} = \prod \Gamma \mathrm{d}z \tag{8}$$

A real imaging system, however, will experience defocusing blur, which is defined by an energy- and z-dependent (3D) Gaussian blur kernel, $PSF(\lambda, z_0)$ centered on a focal plane at z_0.

$$\widetilde{\Gamma}(\lambda, z_0) = \Gamma * PSF(\lambda, z_0) = \mathcal{F}^{-1}\{\mathcal{F}\{\Gamma\} \cdot \mathcal{F}\{PSF(\lambda, z_0)\}\} \tag{9}$$

In this case, $\widetilde{\Gamma}(\lambda, z_0, z)$ defines the contribution of every sample plane to the final image, and the monochromatic image is given by

$$\widetilde{I}(\lambda, z_0) = \prod \widetilde{\Gamma}(\lambda, z_0)\mathrm{d}z \tag{10}$$

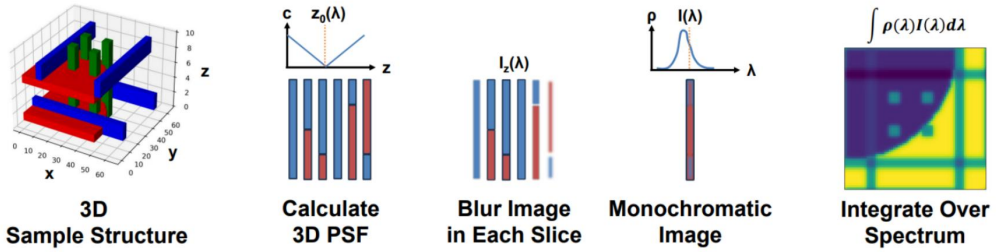

Fig. 3. Proposed algorithm for blurring due to defocusing and chromatic aberration.

This accounts for blurring due to imaging of a sample which is potentially larger than the depth of field of the TXM microscope or misaligned with respect to its focal plane. Note that this approach neglects refraction from the sample, interference, holography, and other wave-optics considerations.

The image resulting from chromatic aberration can then be treated by integrating these monochromatic images over the normalized spectrum of the imaging system, $\rho(\lambda)$

$$I = \int \rho(\lambda)\widetilde{I}\mathrm{d}\lambda \tag{11}$$

3.1 Energy-Dependent Focal Shift

Note that the lens-to-detector distance is constant in all cases. We can then state that $\mathrm{d}d_2 = 0$, which then implies

$$\mathrm{d}d_2 = \Big(1 + \frac{M}{\cos(N\phi)}\Big)\mathrm{d}f_N + \frac{f_N}{\cos(N\phi)}\mathrm{d}M \tag{12}$$

$$+ f_N N M \frac{\tan(N\phi)}{\cos(N\phi)}\mathrm{d}\phi = 0$$

Solving this for $\mathrm{d}M$, we find

$$\mathrm{d}M = -\frac{1}{f_N}\Big((M + \cos(N\phi))\mathrm{d}f_N + f_N N M \tan(N\phi)\mathrm{d}\phi\Big) \tag{13}$$

Plugging this into $\mathrm{d}d_1$ yields

$$\mathrm{d}d_1 = \left(1 + \frac{1}{M^2} + \frac{2}{M\cos(N\phi)}\right)\mathrm{d}f_N + 2f_N\frac{N}{M}\cdot\frac{\tan(N\phi)}{\cos(N\phi)}\mathrm{d}\phi \tag{14}$$

By definition, the focal plane of the imaging system is placed at $d_1 = z_0$ for the nominal λ, and shifts by $\mathrm{d}d_1(\mathrm{d}\lambda)$.

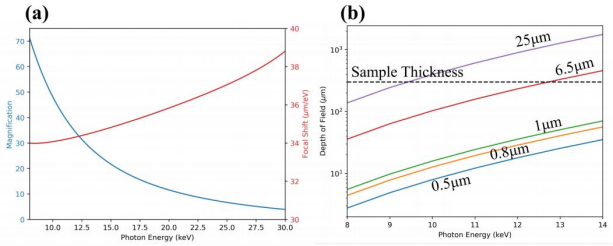

Fig. 4. Chromatic comparison of (a) magnification and focal shift, and (b) depth of field vs different threshold circles of confusion.

Recasting this discussion in terms of photon energy, E, and the energy shift, $\mathrm{d}E$,

$$\mathrm{d}f_N = \phi\cot(N\phi)\mathrm{d}f + \big(f\cot(N\phi) - f\phi f_N N\csc^2(N\phi)\big)\mathrm{d}\phi \tag{15}$$

$$\mathrm{d}\phi = \sqrt{\frac{T}{2R\delta}}\mathrm{d}\delta \tag{16}$$

$$\mathrm{d}f = -\frac{R}{2\delta^2}\mathrm{d}\delta \tag{17}$$

and

$$\mathrm{d}\delta = \Big(\frac{\mathrm{d}\delta}{\mathrm{d}E}\Big)\mathrm{d}E \tag{18}$$

We can now state that the focal plane is at $z_0 = d_1 + \mathrm{d}d_1 = d_1 + \alpha\mathrm{d}E$.

3.2 3D Blur Kernel

The circle of confusion can be defined by

$$c = \frac{Af_N}{z_0 - f_N}\cdot\frac{|z - z_0|}{z} = c(E, z_0, z) \tag{19}$$

and the PSF can be defined by

$$PSF(z, z_0, E) = \frac{1}{\sqrt{2\pi c^2}}\exp\Big(-\frac{r^2}{2c^2}\Big) \tag{20}$$

which is normalized to conserve intensity, where r is the radial position from the center of the blur kernel. It is simpler to define the optical transfer function (OTF) and compute the convolution in Fourier space,

$$OTF(z, z_0, E) = \exp\Big(-\frac{1}{2}k^2c^2\Big) \tag{21}$$

with $k = 2\pi/r$ being the frequency components of the image.

4 Simulation Results

To demonstrate the sensitivity of the CRL imaging system to chromatic aberrations, the following CRL parameters (Table 1) will be assumed, to calculate the focal shift per eV at different wavelengths, as well as the magnification and depth of field changes with energy. These are shown in Figures 4.

Defining an example sample Γ shown in Figure 5 with a z-scale of $30\mu m$ and an x-y-scale of $5\mu m$, the sample is defined in terms of its transmission and has a total volume of $320 \times 320 \times 300\mu m$. Note that, in principle, the transmissions would vary strongly as a function of photon energy due to the material properties of the sample, but

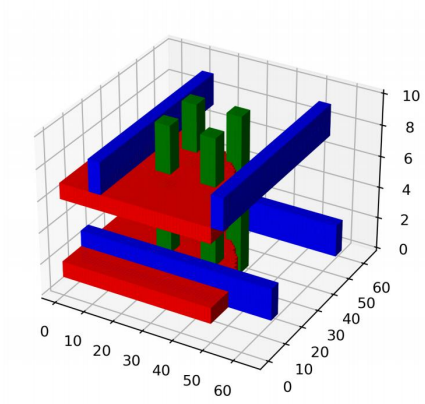

Fig. 5. Example sample geometry with z scale in 30μm and xy-scale 5μm. The red has 50% transmission, blue has 25% transmission and green has 10% transmission. All else is 5% transmission.

in this case, the changes in transmission are neglected to compare results between different energies more easily.

Assuming an 11keV nominal imaging energy, the sample images resulting directly from defocus blur due to the finite depth-of-field are shown for monochromatic imaging in Figure 8. Energy shifts of only $\pm$10eV clearly demonstrate the strong chromaticity of the CRLs, sweeping the focal plane through the entire depth of the sample, bringing different components into focus. In particular, the image component corresponding to the disk can be seen to be most in focus at the $+1$ and $+5$eV shifts (corresponding to changes in the focal plane of $140\mu m$, exactly the distance between the disks defined in the sample Γ) with slight blurring and defocusing between these energies. This behavior is exactly as expected and very sensitive to energy changes within the imaging beam.

The result of this part of the simulation is effectively a focal stack of the sample, if an appropriately sensitive hyperspectral detection scheme were used. Computing the peak signal to noise ratio (PSNR) between $I_{perfect}$ and $I(E)$ with z_0 centered on the front face of the sample, the loss of image resolution due to defocusing is clearly visible in Figure 6a. Another notable feature of this analysis is that higher photon energies give more focused monochromatic images with higher PSNR since the higher photon energies have lower magnification, and thus larger depths of field. In the limit of very high photon energies, where the CRL can no longer magnify significantly, the depth of field will increase significantly and the $I_{perfect}$ image will be recovered.

When a imaging spectrum $\rho(E)$ is defined, a weighted integral of these monochromatic images from the focal stack

TABLE 1
CRL Properties Used by this Work

Property	Symbol	Value	Unit
Number of lenslets	N	50	-
Radius	R	50	μm
Lenslet sepration	T	2	mm

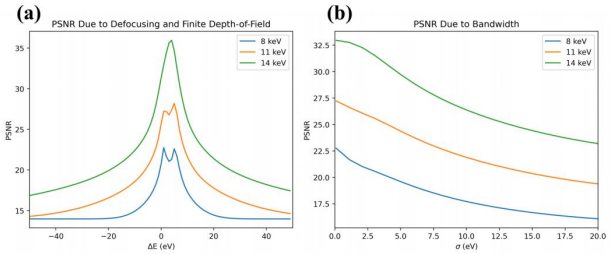

Fig. 6. (a) Loss of resolution in perfectly monochromatic imaging compared to the perfectly in-focused image as a result of the finite depth of field within the sample and energy dependent focal shift. (b) Loss of resolution due to increasing bandwidth with focal plane of central energy centered in sample.

can be readily computed, giving images which sample all the varifocused images with different weights, shown in Figure 7.

Centering ρ at the energy shift corresponding to a focal plane in the middle of the sample, the effect of increasing bandwidth σ on PSNR is shown in Figure 6b. The PSNR drops with increasing bandwidth, as expected, and is maximum for the higher photon energies according to the arguments made previously. However, the decrease in PSNR for polychromatic illumination is less dramatic than in the monochromatic cases where an energy shift occurs. Even though more defocused images are being sampled by the integral in the polychromatic case, the focused images are also being sampled, whereas in the monochromatic case, an energy shift that is too great will completely lose all features of the original sample.

5 Conclusion

This work has constructed a relatively computationally cheap and readily parallelize-able algorithm to compute both the defocusing blur of a transmission x-ray microscope and the effects of chromatic aberration. Moreover, this

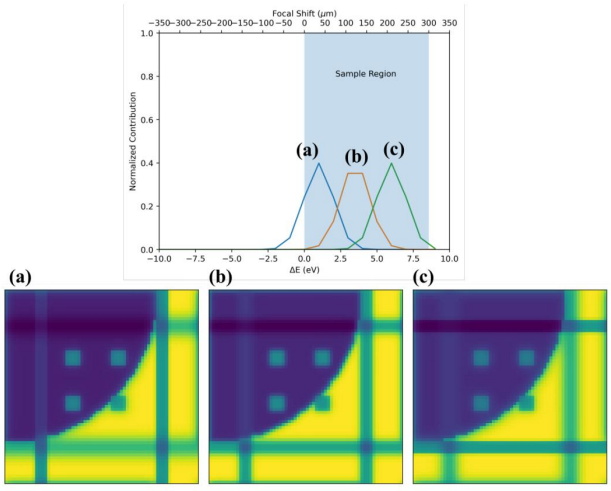

Fig. 7. Spectra and chromatically aberrated images for a microscope focused with nominal 11keV photon energies.

C

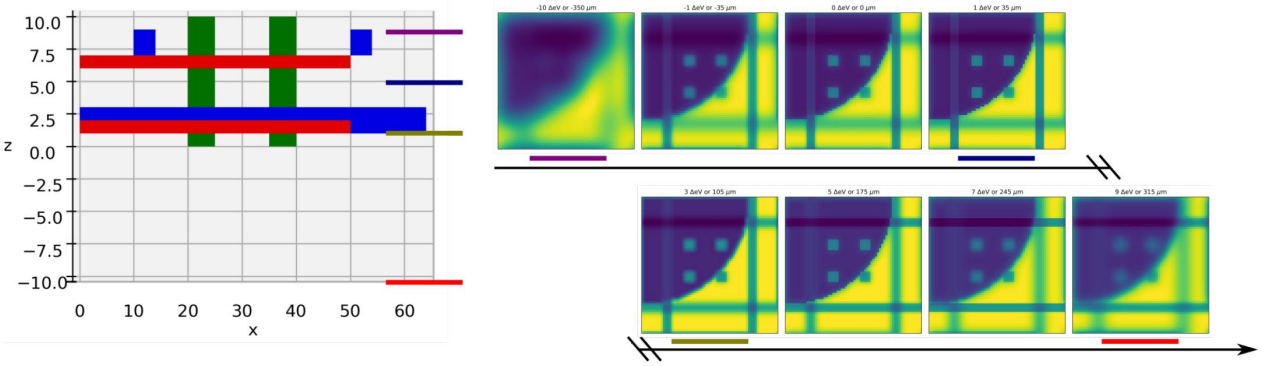

Fig. 8. Demonstration of a focal stack produced by detuning the imaging x-ray energy from the nominal 11keV. This shifts the focal plane through the depth of the sample, bringing different features into and out of focus in these monochromatic images. These are shown in relation to the profile of the samples defined by Γ.

construction is tied directly into the governing physics of CRL optics and can be applied to an photon energy, CRL properties, and microscope length that produces a real image. Further, this construction creates an energy-dependent focal stack prior to the calculation of the chromatically aberrated image, which allows the user to implement a beam spectra of arbitrary shape and to apply further chromatic operations to the images at will. These could include Bragg diffractions, x-ray prisms, additional CRLs and other optics which are chromatic operations that cannot be meaningfully computed for the final, integrated image.

This work captures the intuition of how these transmission images should evolve with microscope design, photon energy, and bandwidth, but has not been compared to experimental results or more precise multi-slice wave-optics simulations. The next steps are to compare these results to those of more precise wave-optics simulations, and to compare them to experimental results if possible. The lack of experimental data is well-explained by the community's avoidance of chromatic aberration by simply monochomating their imaging beams.

In addition to these next steps, this simulation, as constructed, is only accounting for the blurring of the image due to defocus and chromaticity. The end result is a net transmission coefficient, but it remains still to account for the (energy-dependent) changes in the voxel scaling due to the magnification at the image plane, as well as the PSF introduced by the imaging system, including binning into the detector pixels, which could reduce resolution sufficiently to render some of these aberrations invisible.

References

[1] A. Talignani, R. Seede, A. Whitt, S. Zheng, J. Ye, I. Karaman, M. Kirka, Y. Katoh, and Y. Wang, "A review on additive manufacturing of refractory tungsten and tungsten alloys," *Additive Manufacturing*, 2022.

[2] B. Simonds, J. Tanner, A. Artusio-Glimpse, P. Williams, N. Parab, C. Zhao, and T. Sun, "The causal relationship between melt pool geometry and energy absorption measured in real time during laser-based manufacturing," *Applied Materials Today*, 2021.

[3] T. Sun, "Probing ultrafast dynamics in laser powder bed fusion using high-speed x-ray imaging: A review of research at the advanced photon source," *JOM*, 2020.

[4] C. Zhao, N. Parab, X. Li, K. Fezzaa, W. Tan, A. Rollett, and T. Sun, "Critical instability at moving keyhole tip generates porosity in laser melting," *Science*, 2020.

[5] A. Martin, N. Calta, S. Khairallah, J. Wang, P. Depond, A. Fong, V. Thampy, G. Guss, A. Kiss, K. Stone, C. Tassone, J. Weker, M. Toney, T. Buuren, and M. Matthews, "Dynamics of pore formation during laser powder bed fusion additive manufacturing," *Nature Communications*, 2019.

[6] Z. Gan, O. Kafka, N. Parab, C. Zhao, L. Fang, O. Heinonen, T. Sun, and W. Liu, "Universal scaling laws of keyhole stability and porosity in 3d printing of metals," *Nature Communications*, 2021.

[7] S. Boutet and M. Yabashi, *X-Ray Free Electron Lasers and Their Applications*. Springer, 2018.

[8] J. Chang and G. Wetzstein, "Deep optics for monocular depth estimation and 3d object detection," *IEEE*, 2019.

[9] H. Strasburger, M. Bach, and S. Heinrich, "Blur unblurred - a mini tutorial," *i-Perception*, 2018.

[10] H. Nagahara, S. Kuthirummal, C. Zhou, and S. Nayar, "Flexible depth of field photography," *IEEE*, 2011.

[11] H. Merklinger, *The Ins and Outs of Focus*. Self-Published, 2002.

[12] T. Luhmann, H. Hastedt, and W. Tecklenburg, "Modelling of chromatic aberration for high precision photogrametry," *IAPRS*, 2006.

[13] V. Rudakova and P. Monasse, "Precise correction of lateral chromatic aberration in images," *Image and Video Technology*, 2013.

[14] M. Bergkoetter, B. Kruschwitz, S. Bahk, , and J. Feinup, "Measurement of chromatic aberrations using phase retrieval," *J. Opt. Soc. Amer. A*, 2021.

[15] H. Simons, S. Ahl, H. Poulsen, and C. Detlefs, "Simulating and optimizing compound refractive lens-based x-ray microscopes," *J. Synch. Rad*, 2016.